ELSEVIER

International Journal of Heat and Fluid Flow 22 (2001) 156–167

International Journal of
HEAT AND FLUID FLOW

www.elsevier.com/locate/ijhff

# Numerical analysis of fluid flow and heat transfer in periodic wavy channels

B. Ničeno [a], E. Nobile [b,*]

[a] Faculty of Applied Sciences, Section Thermofluids, Delft University of Technology, Delft, Netherlands
[b] Dipartimento di Ingegneria Navale, del Mare e per l'Ambiente, Sezione di Fisica Tecnica, Università di Trieste, Via A. Valerio 10, I-34127 Trieste, Italy

Received 11 May 2000; accepted 23 December 2000

## Abstract

The two-dimensional steady and time-dependent fluid flow and heat transfer through periodic, wavy channels is numerically studied, for a fluid with a Prandtl number of 0.7, by means of an unstructured covolume method. The two geometrical configurations considered, a sinusoidal channel and an arc-shaped channel, are shown to provide little or no heat transfer augmentation, in comparison to a parallel-plate channel, in steady flow regimes at lower values of the Reynolds number. In addition, they both have higher pressure drop than that of the parallel-plate channel under fully developed flow conditions. For the unsteady regime, reached at about $Re = 175$–$200$ for the sinusoidal channel, and $Re = 60$–$80$ for the arc-shaped channel, both geometries exhibit a significant increase in the heat transfer rate, up to three times for the highest Reynolds number investigated. This increase is higher for the arc-shaped flow passage, but is accompanied by a higher friction factor than that of the sinusoidal channel. © 2001 Elsevier Science Inc. All rights reserved.

*Keywords:* Heat transfer enhancement; Covolume method; Unstructured grid

## 1. Introduction

There are several methods used to increase the heat transfer rate in compact heat exchangers (Kakaç et al., 1980). The majority of these methods share a common objective, i.e., to interrupt the boundary layer on the solid surface, and replace it with fluid from the core, thus creating a new boundary layer with an increased temperature gradient. Relevant examples of this technique are offset-fins, vortex generators, louvers, etc. It is desirable to employ the method that gives the minimum pressure drop, and the highest heat transfer rate, though in practice the ease of manufacturability and maintenance has also to be taken into account.

A simple geometry of the flow passage that is relatively easy to produce and can be used to *augment* the heat transfer rate, is the wavy, periodic channel. Wavy or *corrugated* channels, as observed experimentally and numerically (Nishimura et al., 1984, 1990; Wang and Vanka, 1995), usually do not provide any significant heat transfer enhancement if operated in steady regime. However, if a transition to an unsteady regime occurs, a relevant increase of the heat transfer rate is observed. This transition to a time-dependent regime might be *natural* or caused by an external forcing, i.e., oscillatory inflow, acoustic excitation, etc. From the practical point of view, it is the natural transition that is more interesting. The critical Reynolds number, at which bifurcation to time-dependent flow is attained, depends heavily on the geometry of the channel. It is in this unsteady regime that such geometries can be quite effective.

In this work we describe our approach for the numerical study of heat transfer enhancement in periodic corrugated channels. The long-term objective of this research is the design and optimization of heat transfer surfaces, particularly suited for compact heat exchangers, but of general interest for other applications as well. A numerical method used for these calculations must be able to cope with complex geometries, must be able to capture, in an accurate way, the onset of unsteadiness, and finally it should have the capability to portray the evolving velocity and temperature fields in unsteady regimes.

The numerical method employed in this study is based on a time-accurate, control volume (CV) approach. More specifically, the spatial discretization is performed with the so-called *covolume method*, first introduced by Nicolaides (1989, 1992). The main feature of the method is the use of two families of CVs which are mutually orthogonal, and called complementary volumes or covolumes for short. The computational domain is subdivided into a finite number of non-overlapping polygons (CVs) for which a circumcircle can be defined. This family of CVs is called *the primal grid*. The other family of CVs

---

[*] Corresponding author. Tel.: +39-040-676-3507; fax: +39-040-572-033.
*E-mail address:* nobile@univ.trieste.it (E. Nobile).

PII: S0142-727X(01)00074-1

**Notation**

| | |
|---|---|
| $D_{\mathrm{H}}$ | hydraulic diameter ($2H_{\mathrm{av}}$) |
| $f$ | friction factor (Eq. (42)) |
| $\mathbf{f}$ | source term in momentum equation |
| $h$ | length of the Delaunay triangle side |
| $\overline{h}$ | average heat transfer coefficient |
| $H$ | height of the channel |
| $\mathbf{i}$ | unit normal vector in the $x$ (streamwise)-direction |
| $k$ | thermal conductivity |
| $l$ | length of the Voronoi polygon side |
| $L$ | length of the repeating module |
| LMTD | log–mean temperature difference (Eq. (41)) |
| $\mathbf{n}$ | unit normal vector for the triangle side |
| $N$ | number of cells |
| $Nu$ | average Nusselt number (Eq. (38)) |
| $p$ | periodic part of kinematic pressure |
| $P$ | kinematic pressure (pressure divided by density) |
| $Pr$ | Prandtl number ($\nu/\alpha$) |
| $Q$ | heat flux |
| $Re$ | Reynolds number (Eq. (43)) |
| $\mathbf{t}$ | unit tangent vector for the triangle side |
| $T$ | temperature |
| $T_{\mathrm{b}}$ | bulk temperature (Eq. (34)) |
| $\mathbf{u}$ | velocity vector |
| $u$ | velocity component normal to the triangle side |
| $v$ | velocity component tangential to the triangle side |
| $\mathbf{x}$ | position vector |
| $x$ | horizontal (streamwise) component of the position vector |
| $y$ | vertical (normalwise) component of the position vector |

*Greeks*

| | |
|---|---|
| $\alpha$ | thermal diffusivity |
| $\beta$ | overall pressure gradient (Eq. (29)) |
| $\Gamma$ | boundary of cell domain |
| $\varphi$ | scalar potential (pseudo-pressure) |
| $\nu$ | kinematic viscosity |
| $\rho$ | density |
| $\theta$ | normalized temperature (Eq. (33)) |
| $\tau$ | time |
| $\omega$ | scalar vorticity |
| $\boldsymbol{\omega}$ | vorticity |
| $\Omega$ | cell domain |

*Subscripts*

| | |
|---|---|
| av | quantity evaluated at average cross-section $\frac{1}{2}(H_{\max}+H_{\min})$ |
| $i$ | summation over the Delaunay triangle sides |
| in | quantity at inlet |
| $j$ | summation over the Voronoi polygon sides |
| max | quantity evaluated at maximum cross-section |
| min | quantity evaluated at minimum cross-section |
| out | quantity at outlet |
| w | quantity at the wall |

*Superscripts*

| | |
|---|---|
| $m$ | iteration counter |
| $n$ | time level |
| $'$ | primal (Delaunay) grid |
| $''$ | dual (Voronoi) grid |

(dual grid) is obtained by connecting the circumcenters of the primal grid polygons. There are several choices for defining covolumes, the two most widely used being: a pair of two rectangular orthogonal grids or Delaunay triangles as the primal grid and Voronoi polygons as the dual grid. Since complex shapes of passages are of interest, we take advantage of the geometric flexibility offered by unstructured Delaunay grid and use it as a primal grid, and Voronoi as a dual grid.

For the discretization in time a semi-implicit projection scheme (Gresho, 1990) is selected. This approach, in conjunction with the covolume method, guarantees absolute, to machine round-off, mass conservation, thus allowing us to perform, in a robust and reliable way, long-term unsteady simulations.

The geometries considered in this study, of interest to compact heat exchangers, are two different corrugated channels. One is a sinusoidal wavy passage, which was previously examined experimentally by Nishimura et al. (1984, 1990), and numerically studied in Wang and Vanka (1995). The other is an arc-shaped channel, with identical aspect-ratios with the previous one, which was experimentally investigated by Nishimura et al. (1990). Since the channels are periodic in the streamwise direction, it is assumed that, at some distance from the inlet, the flow and thermal fields are periodically fully developed (Patankar, 1977). For this reason, only one period of the flow domain is used to perform the calculations.

The results obtained, from steady to unsteady (periodic and aperiodic) flow regimes for a fluid with a Prandtl number of 0.7, representative of air, agree well with the available experimental data (Nishimura et al., 1984, 1990) and past numerical studies (Wang and Vanka, 1995). In particular, notwithstanding the two-dimensional approximation, the critical value of the Reynolds number at which the bifurcation occurs is satisfactorily predicted.

As expected, the heat transfer rate, summarized by the space- and time-averaged Nusselt number $Nu$, increases significantly in the unsteady regime. In addition, by comparison with the reference case of parallel-plate channel, the results also indicate that both geometries are largely inefficient, with similar Nusselt values and higher pressure drops, in the steady regime. Therefore, while generalization to other unexplored geometries cannot be done, the results suggest that the two corrugated channels represent effective means of heat transfer augmentation in the unsteady/transitional regime, but they should not be operated in the low-$Re$, steady flow conditions.

## 2. Governing equations

In this work, the flow is assumed to be two-dimensional and incompressible. For simplicity, constant thermophysical properties are assumed. Under these assumptions, the governing equations for the fluid flow and energy transport can be written as:

$$\nabla\cdot\mathbf{u}=0, \tag{1}$$

$$\frac{\partial\mathbf{u}}{\partial\tau}+\nabla\cdot(\mathbf{u}\mathbf{u})=-\nabla p+\nu\nabla^2\mathbf{u}+\mathbf{f}, \tag{2}$$

$$\frac{\partial T}{\partial\tau}+\nabla\cdot(\mathbf{u}T)=\alpha\nabla^2 T, \tag{3}$$

where $\mathbf{u}$ is the velocity field, $\tau$ is the time, $\nu$ is the kinematic viscosity, $T$ is the temperature and $\alpha$ is the thermal diffusivity.

## 3. Numerical method

Since the increase of heat transfer is observed, for wavy channels, in the unsteady flow regime, the numerical method should be able to integrate the governing equations accurately and efficiently in time. Methods which usually require inner iterations within a time-step, for example implicit SIMPLE-like methods, were discarded, since they might become time-consuming when solving time-dependent flows. In addition, as pointed out by Manson et al. (1996), the main advantage of fully implicit temporal discretization schemes, i.e., unconditional stability and therefore larger time-steps, is of minor importance for truly unsteady flows, where the time-step is strictly limited on accuracy grounds.

A semi-implicit projection method, as described in Gresho (1990), does not generally require inner iterations in a time-step to satisfy the continuity equation, and therefore it seemed a good choice for the solution of unsteady problems. We also decided to solve the flow equations on unstructured triangular grids, in order to have a complete flexibility in covering any desired geometry of the channel, and also to selectively refine the grid in regions of special interest.

Although several techniques for CV discretization of the fluid flow problem on unstructured grids exist, from our experience not all of them proved suitable for our purpose.

It is well known that the problem of spurious pressure field, which might occur in numerical simulations of incompressible flows, can be effectively eliminated by using the staggered grid approach. In this respect, there exist several possibilities of placing the unknown pressure and velocity components to achieve *staggering*. For example, in (Thomadakis and Leschziner, 1996) the velocity components are placed on the triangle (or polygons in general) nodes, and the pressure in the triangle centroid. The velocity components are then discretized, in the *centroid dual* of the primary grid, with the standard Finite Volume approach, and mass conservation is sought on the primary grid to obtain the equations for velocity corrections. Such a scheme works well with the SIMPLE algorithm but, according to our experience, if it is combined with the projection method, a single velocity correction step does not always bring the mass error to zero. In other words, the link between the velocities and pressure is rather weak.

Another very interesting technique of staggering the velocities is described by Hwang (1995a,b). The velocity components are placed on the triangle sides, and the pressure is placed in the triangle centroid. This discretization technique provides a strong link between velocities and pressure, and, when combined with the projection method, a single velocity correction step is able to bring the mass error down to the order of machine round-off. However, a drawback of this method is the situation, which sometimes occur, in which the velocity lies parallel to the triangle side. That velocity becomes practically *invisible* to the pressure corrections. This situation was observed, for example, when calculating buoyant flows, i.e., the natural convection side-heated cavity. A similar approach of that of Hwang, and called *side-centered scheme*, is described in Ridia et al. (1997).

To the best of our knowledge, there are not many studies in which the projection method is successfully applied on unstructured triangular grids. Botta and Hempel (1996) have chosen to place the velocities on the triangle centroids, and the pressures on the triangle nodes. With this arrangement it is easy to calculate the pressure gradient and satisfy the mass conservation. The only caveat of the method is its relative complexity, since it needs three different grids (two triangular and one polygonal) to solve the governing equations in two dimensions. The method described by Despotis and Tsangaris (1996), uses only one grid to solve the governing equations, but it seems that it has been applied only on regular triangular grids, i.e., grids with equilateral sides. A general fractional-step projection algorithm, for hybrid unstructured finite volume grids (i.e., grids composed of triangles and quadrilaterals), has been recently presented by Kobayashi et al. (1999). It was proved that the method attains a second-order of accuracy, on arbitrary unstructured hybrid meshes, for the incompressible two-dimensional steady version of the Navier–Stokes equations.

In this work, the discretization is performed with the so-called complementary volume (or covolume for short) method, first introduced by Nicolaides (1989, 1992) and subsequently applied by Hall et al. (1991), Cavendish et al. (1992, 1994) and Hall and Porsching (1996). The main feature of the method is the use of two sets of CVs or cells, with the property that the edges of each set of cells are perpendicular to the faces of the other set. In two dimensions, an illustrative example of covolumes is the staggered Cartesian grid. Another example of covolumes in two dimensions consists of Delaunay–Voronoi grids. Other possibilities exist, like trapezoidal grids, and combinations of Cartesian, triangular and trapezoidal grids. Although these combinations can be useful in some circumstances, in this work we considered only the Delaunay–Voronoi pairs, because of their geometrical flexibility, conservation properties (Perot, 2000), and relative ease of generation.

It is interesting to note, at this point, that there is widespread acceptance of the idea of limited flexibility of the covolume approach, using the Delaunay–Voronoi grid pairs (see Ridia et al., 1997), because of the orthogonality constraint, in particular when considering complex shapes and adaptive grids. Such misconception is based on the assumption that the generation of Delaunay–Voronoi grids has to be *centroid-based*. This is not true, since grid generators *circumcenter-based* also exist (Ničeno, 1997), which produce high quality grids and yet are flexible enough to allow for grid adaptation. Furthermore, as pointed out in (Perot, 2000), the covolume method does not necessarily require that the cell circumcenters be located within the cell itself, or that the mesh be a Delaunay tesselation. Highly distorted grids, i.e., grids where a significant portion of the cell circumcenters lies outside the respective cell, impact the accuracy, but *not* the conservation properties, of the method (Perot, 2000).

The primitive variables in the covolume method are the velocity components normal to the sides of one set of cells, and the pressure. As illustrated in Fig. 1, velocity components are located at the intersections of the two set of grids, normal to the sides of one set (which is then referred to as the *primal grid*), and parallel to the sides of the remaining set (*dual grid*) of CVs. Pressure, temperature and any additional scalar variables, are defined on the nodes of the dual grid.

This type of discretization can be considered as the generalization of the well-known MAC method on triangular grids.

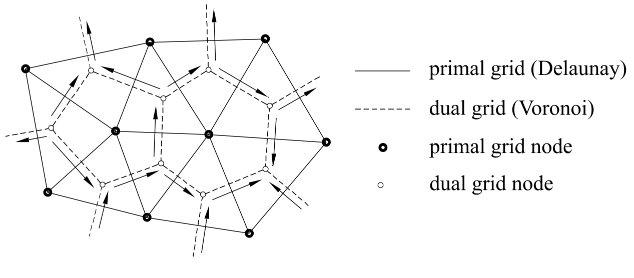

Fig. 1. Placement of primitive variables on the Delaunay–Voronoi grid-pair.

Therefore, the method presented has the geometric flexibility of the unstructured triangular grids, while preserving the conservation properties of a staggered grid arrangement.

### 3.1. Spatial discretization

We describe first the spatial discretization of the momentum and energy equations, and then the temporal discretization, which is formally independent from the former.

#### 3.1.1. Continuity and vorticity

The continuity equation is never solved explicitly during the calculations. However, its discretization is used when computing the pressure, and when checking for mass conservation.

Integrating (1) over the primal CV, and applying Gauss theorem, gives

$$\int_{\Omega'} \nabla \cdot \mathbf{u} \, \mathrm{d}\Omega' = \int_{\Gamma'} \mathbf{u} \cdot \mathbf{n} \, \mathrm{d}\Gamma' \approx \sum_{i=1}^{N'} u_i n_i h_i, \tag{4}$$

where with reference to Fig. 2(a), $\mathbf{n}$ denotes the unit outward vector normal to the primal cell side, $u_i$ is the velocity component normal to the triangle side, $h_i$ is the length of the primal cell side, and $n_i$ represents the discretized normal on the cell side: its possible values are $+1$ or $-1$, depending if the velocity is oriented outward or inward of the primal control volume. $N'$ is the number of sides of the primal cell, and when the Delaunay triangulation is used as the primal grid, it has always a value of 3.

The discretization of vorticity is used for the transformation of the viscous stress tensor in the momentum equation (2) into a form more suitable for discretization by the covolume method. The scalar vorticity $\omega = -\omega_z$ is computed at each node of the primal grid (see Fig. 2(b)), and can be approximated, over the dual grid cell, by

$$\omega = \frac{1}{\Omega''} \int_{\Gamma''} \mathbf{u} \cdot \mathbf{t} \, \mathrm{d}\Gamma'' \approx \frac{1}{\Omega''} \sum_{j=1}^{N''} u_j t_j l_j, \tag{5}$$

where $\mathbf{t}$ is the unit vector tangent to $\Gamma''$, traversing it in the anticlockwise direction, $l_j$ is the length of the dual (Voronoi) cell side, and $t_j$ is the discretized tangent vector on the cell side: its possible values are $+1$ or $-1$, depending if the velocity is traversing the node in the anticlockwise or clockwise sense. $N''$ is the number of dual cell sides, and in our case, where the Voronoi polygons are used as dual cells, it may vary from node to node.

#### 3.1.2. Momentum equation

The momentum equation is approximated at each intersection of the primal and dual grid, which is, for the case of Delaunay–Voronoi grid, the midpoint $P$ of each triangle side (see Fig. 3(a)). Since the primitive variables are the velocity components normal to the triangle side, we have to express the momentum equation as a function of the normal components of velocities of adjacent triangle sides. For that purpose, the following definition from the vector analysis is employed

$$\nabla^2 \mathbf{u} = \nabla(\nabla \cdot \mathbf{u}) - \nabla \times (\nabla \times \mathbf{u}) = -\nabla \times \boldsymbol{\omega}. \tag{6}$$

Substituting Eq. (6) into Eq. (2), the following form of the Navier–Stokes equation is obtained

$$\frac{\partial \mathbf{u}}{\partial \tau} + \nabla \cdot (\mathbf{u}\mathbf{u}) = -\nabla p - \nu \nabla \times \boldsymbol{\omega} + \mathbf{f}. \tag{7}$$

In order to obtain the equation for the normal velocity component, the Navier–Stokes equation has to be projected in the

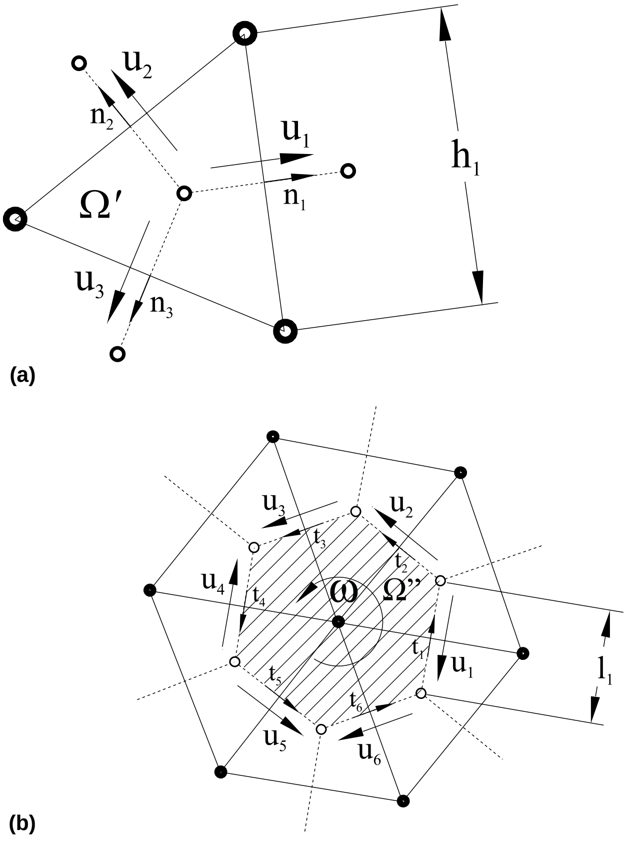

Fig. 2. Discretization of: (a) continuity; (b) vorticity.

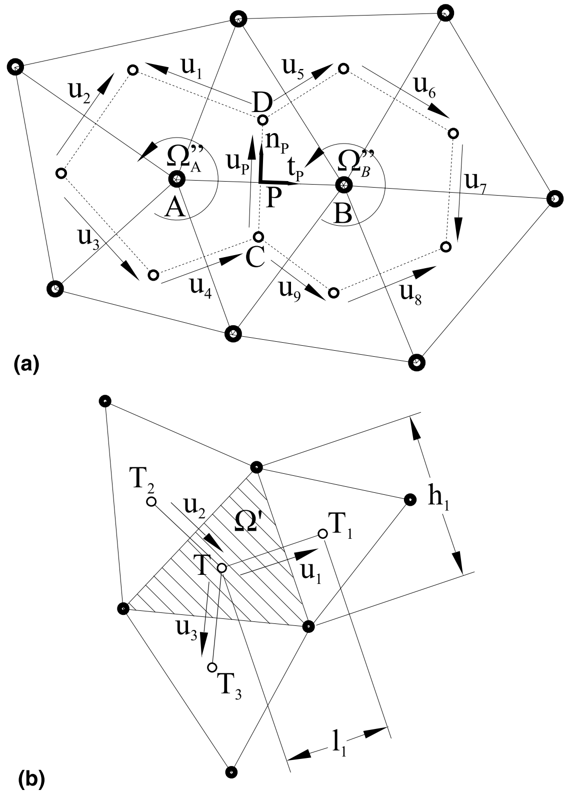

Fig. 3. Discretization stencils: (a) momentum equation; (b) energy equation.

normal direction. Multiplying Eq. (7) by $\mathbf{n}_P$, the unit vector normal to the triangle side $AB$, we obtain a *scalar* version of the momentum equation (Cavendish et al., 1994)

$$\frac{\partial u_P}{\partial \tau} + \nabla(\mathbf{n}_P \cdot \mathbf{u}) \cdot \mathbf{u} = -\frac{\partial p}{\partial \mathbf{n}_P} + v\frac{\partial \omega}{\partial \mathbf{t}_P} + \mathbf{f} \cdot \mathbf{n}_P. \tag{8}$$

This is the form of the Navier–Stokes equation which is most suitable for subsequent discretization with the covolume method.

The convective fluxes are obtained by an area-weighted interpolation, as described in Hall et al. (1991), of the convective terms evaluated for adjacent triangles. With reference to Fig. 3(a)

$$\nabla(\mathbf{n}_P \cdot \mathbf{u}) \cdot \mathbf{u}\,|_P \approx \frac{\Omega'_C}{\Omega'_C + \Omega'_D}\nabla(\mathbf{n}_P \cdot \mathbf{u}) \cdot \mathbf{u}\,|_C + \frac{\Omega'_D}{\Omega'_C + \Omega'_D}\nabla(\mathbf{n}_P \cdot \mathbf{u}) \cdot \mathbf{u}\,|_D, \tag{9}$$

where $\Omega'_C$ and $\Omega'_D$ are areas of triangles $C$ and $D$ adjacent to triangle side $AB$.

The corresponding convective term for each of the triangles is calculated in the following way

$$\nabla(\mathbf{n}_P \cdot \mathbf{u}) \cdot \mathbf{u}\,|_{\Omega'} = \frac{1}{\Omega'}\int_{\Gamma'}(\mathbf{n}_P \cdot \mathbf{u})(\mathbf{n} \cdot \mathbf{u})\,\mathrm{d}\Gamma' \approx \frac{1}{\Omega'}\sum_{i=1}^{N'}(\mathbf{n}_P \cdot \mathbf{u}_i)u_i n_i h_i, \tag{10}$$

where $i$ implies summation over triangle sides, $N'$ is the number of triangle sides (which is always three) and $\mathbf{u}_i$ are the velocity vectors on triangle sides.

The pressure term is approximated as

$$\frac{\partial p}{\partial \mathbf{n}_P} \approx \frac{p_C - p_D}{l}, \tag{11}$$

where $p_C$ and $p_D$ are the pressures in the triangles adjacent to the side $P$ (see Fig. 3(a)).

The viscous term is obtained by introducing the discretized vorticity, given by (5), into the viscous part of (8)

$$v\frac{\partial \omega}{\partial \mathbf{t}_P} \approx v\frac{\omega_B - \omega_A}{h} = \frac{\frac{1}{\Omega''_B}\sum_{j=1}^{N''_B} u_j t_j l_j - \frac{1}{\Omega''_A}\sum_{j=1}^{N''_A} u_j t_j l_j}{h}. \tag{12}$$

### 3.1.3. Reconstruction of the velocity field

It is obvious from Eqs. (9)–(12), that the normal component of the velocity at $P$ is a function of the normal velocity components of the sides which contain node $A$ or $B$. However, the tangential components are also needed for the evaluation of the convective fluxes in Eq. (10). These unknown tangential components of the velocity can be reconstructed from the known normal components. In practice, however, we treat the convective fluxes explicitly and therefore, when evaluating (10), the tangential components for that purpose are known.

The method we used for the reconstruction of the velocity field follows directly from Nicolaides (1989) and Hall et al. (1991). With reference to Fig. 4, the tangential velocity component can be obtained from the (reconstructed) velocity values at points $C$ and $D$, from the following expression

$$v_P \approx \frac{1}{2}(\mathbf{u}_C + \mathbf{u}_D) \cdot \mathbf{t}_P. \tag{13}$$

The velocities $\mathbf{u}_C$ and $\mathbf{u}_D$ are obtained by assuming that they are constant in each triangle. Following that assumption, the following relations hold:

$$u_1 = \mathbf{u}_D \cdot \mathbf{n}_1, \tag{14}$$

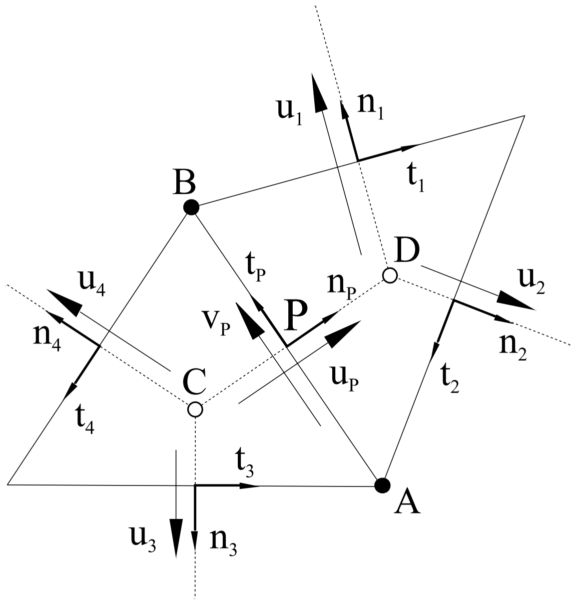

Fig. 4. Evaluation of the tangential component $v_P$.

$$u_2 = \mathbf{u}_D \cdot \mathbf{n}_2, \tag{15}$$

$$u_3 = \mathbf{u}_C \cdot \mathbf{n}_3, \tag{16}$$

$$u_4 = \mathbf{u}_C \cdot \mathbf{n}_4, \tag{17}$$

where $u_1$, $u_2$, $u_3$ and $u_4$ are the velocity components normal to the triangle sides which enclose node $P$ (see Fig. 4). When Eqs. (14)–(17) are solved for $\mathbf{u}_C$ and $\mathbf{u}_D$ the solution of the following form is obtained:

$$\mathbf{u}_C = \frac{u_4\mathbf{t}_3 - u_3\mathbf{t}_4}{\mathbf{t}_3 \cdot \mathbf{n}_4}, \tag{18}$$

$$\mathbf{u}_D = \frac{u_2\mathbf{t}_1 - u_1\mathbf{t}_2}{\mathbf{t}_1 \cdot \mathbf{n}_2}. \tag{19}$$

The extension of the covolume method to three-dimensional problems has already been proposed in Cavendish et al. (1994), where the Delaunay tetrahedrons and Voronoi polyhedra are used as the primal and dual mesh, respectively. Vorticity, which is the basis for the discretization of viscous terms, is defined on each face of the Voronoi polyhedron, around the tetrahedron edge.

The difficulties associated with the generation of a pair of Delaunay–Voronoi tesselations in three dimensions, are somehow mitigated by the fact that the covolume method can still be applied, though at reduced accuracy, in degenerate cases, as shown in Cavendish et al. (1994). These situations correspond to Voronoi polyhedra which have faces of zero area or edges of zero length, or collapsed tetrahedra with arbitrary small, and in extreme cases even zero, volume, but well-proportioned triangular faces, which are termed *slivers*.

### 3.1.4. Energy equation

The temperature unknowns are associated with the triangle circumcenters. The discretization of the energy equation follows the standard approach of the CV method, i.e., integrate the governing equation over the CV, and apply Gauss theorem to replace area integrals (volume integrals in three dimensions) with boundary line integrals (surface integrals in three dimensions). This procedure is equivalent to integrating heat fluxes over the faces of the CV. The calculation of the heat fluxes on the Delaunay–Voronoi pair is very simple, because of the orthogonality of the grids.

Therefore, the integration of Eq. (3), on the primal (Delaunay) grid, takes the form

$$\int_{\Omega'} \frac{\partial T}{\partial \tau}\, \mathrm{d}\Omega' + \int_{\Gamma'} (\mathbf{u}T) \cdot \mathbf{n}\, \mathrm{d}\Gamma' = \alpha \int_{\Gamma'} \nabla T \cdot \mathbf{n}\, \mathrm{d}\Gamma'. \tag{20}$$

The convective term is calculated by

$$\int_{\Gamma'} (\mathbf{u}T) \cdot \mathbf{n}\, \mathrm{d}\Gamma' \approx \sum_{i=1}^{N'} u_i \bar{T}_i h_i, \tag{21}$$

where $i$ implies summation over triangle sides, $\bar{T}_i$ are temperatures at triangle sides, and can be obtained in a variety of ways. In this work, an area-weighted interpolation was used, resulting (see Fig. 3(b))

$$\bar{T}_i = \frac{\Omega'_i}{\Omega'_i + \Omega'} T_i + \frac{\Omega'}{\Omega'_i + \Omega'} T, \tag{22}$$

where $\Omega'$ is the area of the shaded triangle in Fig. 3(b) and $\Omega'_i$ represents the area of the neighboring triangle.

This interpolation, as well as that given in (9), corresponds to central differencing used in conventional finite difference discretization. It is evident from Eq. (21) that for the calculation of the convective heat fluxes, only the velocity components normal to the triangle sides are needed.

The diffusive term is given by (see Fig. 3(b))

$$\alpha \int_{\Omega'} \nabla T \cdot \mathbf{n}\, \mathrm{d}\Gamma' \approx \alpha \sum_{i=1}^{N'} (T_i - T) \frac{h_i}{l_i}. \tag{23}$$

### *3.2. Discretization in time*

#### *3.2.1. Fluid flow equations*

For the discretization in time, a semi-implicit, second-order projection method, described in Gresho (1990), is used. This method was chosen because it is characterised by computational efficiency in the temporal integration, which is very important for the present work, where the main interest is to accurately portrait unsteady flow dynamics and heat transfer.

In the projection method, the first stage of the integration consists of solving the momentum equation for an intermediate velocity field given by

$$\frac{\tilde{\mathbf{u}}^{n+1} - \mathbf{u}^n}{\Delta\tau} = -\nabla p^n + \frac{3}{2}\mathbf{H}_{\mathbf{u}}^n - \frac{1}{2}\mathbf{H}_{\mathbf{u}}^{n-1} + \frac{\nu}{2}\nabla^2(\tilde{\mathbf{u}}^{n+1} + \mathbf{u}^n), \tag{24}$$

where $\tilde{\mathbf{u}}^{n+1}$ is the tentative velocity field and $\mathbf{H}_{\mathbf{u}} = -\nabla \cdot (\mathbf{uu})$. In (24), the convective term is discretized by a second-order, explicit Adams Bashfort method, while the diffusive term is discretized with the Crank–Nicolson scheme. This tentative velocity field, $\tilde{\mathbf{u}}^{n+1}$, is in general not satisfying the continuity equation. This step is followed by the solution of a Poisson's equation for the scalar potential (pseudo-pressure) $\varphi$

$$\nabla^2\varphi = \nabla\tilde{\mathbf{u}}^{n+1}. \tag{25}$$

The left-hand side of (25) is discretized in the same way as the diffusive term of the energy equation (23), with $\alpha = 1$, and the discretization of the right-hand side of (25) is given by (4).

Finally the normal velocity components at the new time-step can be calculated from

$$\mathbf{u}^{n+1} = \tilde{\mathbf{u}}^{n+1} - \nabla\varphi. \tag{26}$$

These velocity components satisfy the divergence-free condition, and therefore the tangential velocity components can be safely reconstructed to complete the calculation of the flow field.

The pressure is updated with

$$p^{n+1} = p^n + \frac{3}{2}\frac{\varphi}{\Delta\tau}. \tag{27}$$

#### *3.2.2. Energy equation*

For the energy equation, as for the momentum equation, the non-linear term is discretized with the second-order explicit Adams–Bashfort scheme, and the diffusive term is discretized with the Crank–Nicolson scheme

$$\frac{T^{n+1} - T^n}{\Delta\tau} = \frac{3}{2}H_T^n - \frac{1}{2}H_T^{n-1} + \frac{\alpha}{2}\nabla^2(T^{n+1} + T^n), \tag{28}$$

where $H_T = -\nabla \cdot (\mathbf{u}T)$.

### *3.3. Solution of linear systems*

The linear systems resulting from the present discretization are all banded and sparse. However, there is a fundamental difference between the systems resulting from the discretization of velocity and temperature equations on the one side, and the system resulting from the discretization of the scalar potential $\varphi$.

The linear systems resulting from the discretization of the Helmholtz-type momentum and energy equations, are very well conditioned (diagonally dominant), and suitable for solving with iterative solvers (CG, CR, BiCG, GMRES, etc.). In this work the BiCG (BiConjugate Gradient) method was used, because the system resulting from discretization of the momentum equation is non-symmetric. The number of iterations per time-step was usually below 10 for the solution in the unsteady regime, and almost insensitive to the number of unknowns.

On the other side, the discretization of the pressure correction equation (25), with Neumann and periodic boundary conditions, results in a very poorly conditioned linear system. As a consequence, when iterative methods were used, it resulted in a large number of iterations per time-step, as also experienced by Huser and Biringen (1992). For this reason, this system was solved with a direct solver based on LU decomposition.

The computer program used in this study was written in standard C, and compiled with the GNU C compiler on a Linux system. All the computations were performed on a PC with Intel Pentium II Celeron processor at 400 MHz.

On the finest grid reported here (12,500 triangles) the speed of the code was 41.5 μs per cell and time-step. The most time consuming part of the code, as expected, is the direct solution of the pseudo-pressure equation, which takes about 85% of the computational time.

## 4. Geometrical configuration and computational details

The two geometries shown in Fig. 5 were examined, as representative of typical corrugated channels adopted for heat transfer augmentation.

The sine-shaped wavy channel was previously examined numerically by Wang and Vanka (1995), and experimentally by Nishimura et al. (1984, 1990). The fluid flow and mass transfer in the arc-shaped wavy channel was experimentally studied by Nishimura et al. (1990).

We studied the flow and temperature fields under the assumption of fully developed flow, which means that the flow pattern repeats itself from module to module, and the heat transfer coefficient has reached its asymptotic value. In such circumstances it is sufficient to analyze only one segment (module) of the geometry (Patankar, 1977).

We did not analyze in detail, for the unsteady regime, the effects of including, in the computational domain, more than

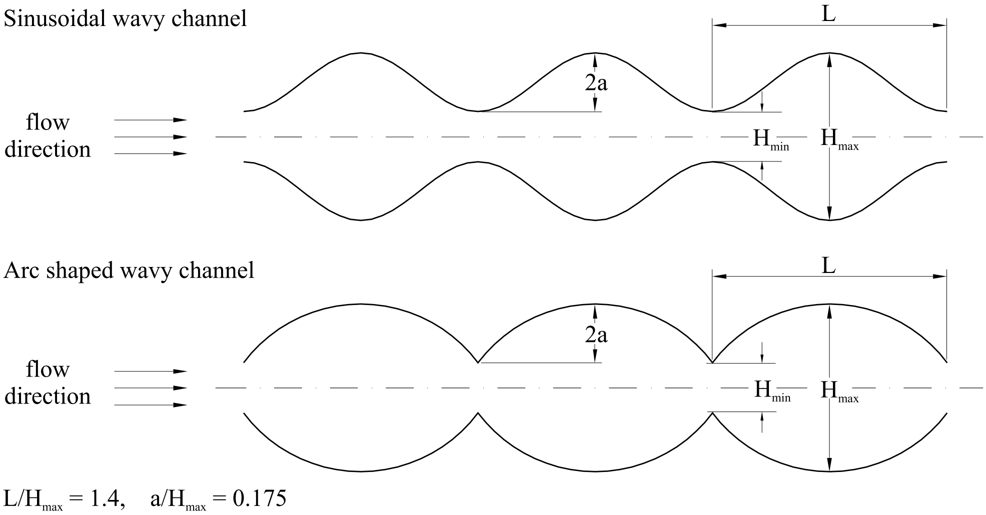

Fig. 5. Geometrical configuration of the corrugated channels.

one repeating module. However, several other studies (Wang and Vanka, 1995; Wang et al., 1996; Amon and Mikic, 1990), have demonstrated the adequacy of using only one of the modules as the computational domain. For example, in Wang and Vanka (1995), it was proved that, for the sinusoidal wavy channel considered also here, increasing the length of the computational domain up to three repeating modules had no effect in the instantaneous flow patterns, which were the same in each module. In Wang et al. (1996), a comparison of the time-traces of streamwise velocity component and temperature, obtained for a computational domain of length $L$ and length $3L$, respectively, did not reveal any difference.

The pressure field in the fully developed region can be expressed (Patankar, 1977) as the linear combination of the local pressure, and the overall pressure drop

$$P(x,y,\tau) = p(x,y,\tau) + \beta x, \tag{29}$$

where the local component $p(x,y,\tau)$ repeats itself from module to module. The overall pressure gradient $\beta$ is introduced in the momentum equation (2) as the source term $\mathbf{f}$ in the streamwise direction

$$\mathbf{f} = \beta \cdot \mathbf{i}, \tag{30}$$

where $\beta$ is the prescribed pressure drop, and $\mathbf{i}$ is the unit vector in the $x$ (streamwise) direction.

A no-slip boundary condition for velocity is enforced on the walls of the channels, and a periodic boundary condition is applied at the inflow and outflow of the computational domain (see Fig. 5)

$$\mathbf{u}(\mathbf{x},\tau) = 0, \quad \mathbf{x} \in \mathbf{x}_{\mathrm{w}} \quad \tau \geqslant 0, \tag{31}$$

$$\mathbf{u}(\mathbf{x}_{\mathrm{in}},\tau) = \mathbf{u}(\mathbf{x}_{\mathrm{out}},\tau) \quad \tau \geqslant 0. \tag{32}$$

For the temperature field, there are two fundamental types of boundary conditions which can be prescribed on the walls: constant heat flux, or constant temperature. In the present work, the latter was used throughout.

For the solution of the temperature field, a non-dimensional temperature is introduced

$$\theta(\mathbf{x},\tau) = \frac{T(\mathbf{x},\tau) - T_{\mathrm{w}}}{T_{\mathrm{b}}(x,\tau) - T_{\mathrm{w}}}, \tag{33}$$

where $T_{\mathrm{w}}$ is the wall temperature, and $T_{\mathrm{b}}$ is the bulk temperature, defined by

$$T_{\mathrm{b}}(x,\tau) = \frac{\int_H \mathbf{u}T(\mathbf{x},\tau) \cdot \mathbf{n}\,\mathrm{d}y}{\int_H \mathbf{u} \cdot \mathbf{n}\,\mathrm{d}y}. \tag{34}$$

The result of this normalization is the periodicity condition for the non-dimensional temperature field

$$\theta(0,y,\tau) = \theta(L,y,\tau) = \theta(2L,y,\tau) = \ldots, \tag{35}$$

where $L$ is the length of the periodic (repeating) module.

The solution of the temperature field, with this normalization, presents some difficulties. One is due to the fact that the bulk temperature distribution $T_{\mathrm{b}}(x,\tau)$ is not known a priori. In particular, it can be shown (Murthy and Mathur, 1997) that, for the constant temperature boundary condition, the solution of the energy equation in its non-dimensional form represents a non-linear problem. Several authors like Wang and Vanka (1995), Wang et al. (1996) and Murthy and Mathur (1997) circumvented this difficulty by linking the non-dimensional temperature field with the bulk temperature in an iterative fashion. However, our desire was to avoid, whenever possible, inner iterations in a time-step, or otherwise the overall computing time could become too large for an unstructured grid approach.

A second difficulty is the evaluation of (34) on the unstructured triangular grid.

Our approximate strategy was to use the normalization procedure (35) to scale the temperature profile, from the outlet of the module, and copy it to the inlet, as the profile for the new iteration of the linear solver for the energy equation. This can be expressed, indicating with the superscript $m$ the iteration counter, by

$$T^m(0,y,\tau) = \left(\frac{T_{\mathrm{b}}(0,\tau) - T_{\mathrm{w}}}{T_{\mathrm{b}}^{m-1}(L,\tau) - T_{\mathrm{w}}}\right)\left(T^{m-1}(L,y,\tau) - T_{\mathrm{w}}\right) + T_{\mathrm{w}}, \tag{36}$$

which is the consequence of (35) and the definition of bulk temperature (34). Since the time-steps, and consequently the temperature variations, were relatively small, this did not affect the overall efficiency of the solver. One variable remains to be set, and that is the bulk temperature at the inflow $T_{\mathrm{b}}(0,\tau)$. In our calculations we have set it to a constant, arbitrary value, different from $T_{\mathrm{w}}$. The choice of the value for the bulk temperature is irrelevant for the later calculation of $Nu$, since it is obtained from the non-dimensional temperatures.

At the outflow, a standard Neumann boundary condition was used

$$\frac{\partial T(L,y,\tau)}{\partial \mathbf{i}} = 0. \tag{37}$$

In all the calculations, the wall temperature $T_w$ is set to 0.

Although the grid is unstructured and the calculation of the bulk temperature is cumbersome inside the domain, this is not the case for the outflow boundaries, since the triangle sides on these boundaries are normal to the $x$-axis. Therefore it is straightforward to calculate the bulk temperature at the outflow which appears in Eq. (36).

The heat transfer rate is summarized by the Nusselt number, which is defined as

$$Nu = \frac{\overline{h} D_{\mathrm{H}}}{k} \tag{38}$$

where $D_{\mathrm{H}}$ is the hydraulic diameter, defined as twice the average channel height $H_{\mathrm{av}}$. The space- and time-averaged heat transfer coefficient $\overline{h}$, is given simply as a Riemann sum, where $N_\tau$ is the number of time-steps used to collect time-averaged quantities

$$\overline{h} = \frac{1}{\Delta\tau}\int_{\tau}^{\tau+\Delta\tau} \frac{Q}{(2L)(\mathrm{LMTD})}\,\mathrm{d}\tau = \frac{1}{N_\tau}\sum_{N_\tau} \frac{Q}{(2L)(\mathrm{LMTD})} \tag{39}$$

with $Q$ being the instantaneous, total heat flux in the module

$$Q = (T_{\mathrm{b}}(0,\tau) - T_{\mathrm{b}}(L,\tau)) \int_H \mathbf{u}\cdot\mathbf{n}\,\mathrm{d}y \tag{40}$$

and LMTD the log–mean temperature difference in the module

$$\mathrm{LMTD} = \frac{(T_{\mathrm{w}} - T_{\mathrm{b}}(L,\tau)) - (T_{\mathrm{w}} - T_{\mathrm{b}}(0,\tau))}{\ln((T_w - T_{\mathrm{b}}(L,\tau))/(T_w - T_{\mathrm{b}}(0,\tau)))}. \tag{41}$$

Recognizing the approximate treatment of the boundary conditions for the energy equation, we have checked for the standard case of fully developed flow and heat transfer in a parallel-plate channel, in which case the Nusselt number, Eq. (38), is equal to 7.54 (Shah and London, 1978). For $Re = 180$, a value of the same order of $Re$ considered for the corrugated channels, the values of $Nu$ obtained on three grids ranging from coarse (650 nodes), medium (2564 nodes) to fine (3478 nodes), were 7.74, 7.56 and 7.55, respectively. These results indicate that, for steady regimes, our approach gives satisfactory results. For unsteady regimes, we will show that, for the sine-shaped channel, the predicted values of the heat transfer rate agree well with those of Wang and Vanka (1995). These results indicate an acceptable level of accuracy of our approach also for time-dependent regimes.

The time-averaged friction factor was computed according to its standard definition:

$$f = \frac{\beta H_{\mathrm{av}}}{2\rho u_{\mathrm{av}}^2}, \tag{42}$$

where $u_{\mathrm{av}}$ is the time-averaged mean velocity in the channel.

The Reynolds number is defined in the usual way

$$Re = \frac{u_{\mathrm{av}} H_{\mathrm{av}}}{\nu}. \tag{43}$$

## 5. Results and discussion

The two different wavy channels of Fig. 5 were studied, for a Prandtl number of 0.7, representative of air, for a range of Reynolds numbers which give rise to either steady or time-dependent, but not turbulent, regime.

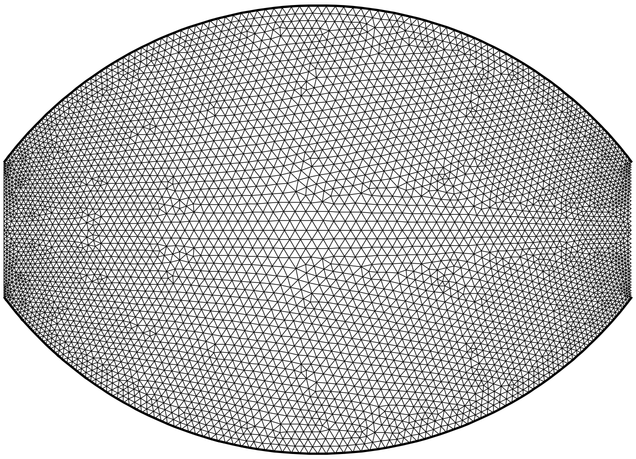

Fig. 6. Grid for the arc-shaped channel.

Table 1
Results of grid independence tests for the overall heat transfer

| Sine-shaped channel | $Nu = \overline{h}D_{\mathrm{H}}/k$ | |
|---|---|---|
| | $Re \approx 25$ | $Re \approx 175$ |
| Grid 1 – 5664 cells | 7.888 | 9.156 |
| Grid 2 – 7588 cells | 7.895 | 9.164 |
| Grid 3 – 10,136 cells | 7.897 | 9.167 |
| Arc-shaped channel | $Re \approx 19$ | $Re \approx 61$ |
| Grid 1 – 6968 cells | 7.082 | 7.218 |
| Grid 2 – 9344 cells | 7.091 | 7.228 |
| Grid 3 – 12,500 cells | 7.096 | 7.233 |

Symmetric grids were used for the computations, to ensure that if any asymmetry in the flow field occurs, it could not be attributed to the grid, but to the natural transition to unsteady flow. The grids adopted are characterised by 5664 and 6968 cells for the sine-shaped channel and the arc-shaped channel, respectively. The grid for the arc-shaped channel is depicted in Fig. 6. All the results shown in this section were obtained with these grids.

A grid refinement study was performed, for both channels and two values of the Reynolds number, in order to assess the accuracy of the results presented. A summary of the grid refinement study is given in Table 1. From the results, it can be seen that the values of $Nu$ obtained on different grids differ by less than 0.25%, thus demonstrating the adequacy of the grids adopted, and the numerical accuracy of the method.

The initial conditions were either those corresponding to a quiescent isothermal fluid, or the flow and temperature fields obtained from a lower value of $Re$. In order to trigger the possible bifurcation to the unsteady regime, and thus reduce the length of the initial transient, the flow was perturbed by adding, for a certain number of time-steps, a randomly distributed force field.

### 5.1. Steady regime

Although in the steady regime the flow is symmetrical about the horizontal centerline, requiring the solution for only one of the halves, the complete domain, between the two walls, was solved in order to locate the approximate value of $Re$ at which the transition from the steady regime to unsteady conditions occurs.

The discretized equations were integrated for a sufficiently long time until time invariant flow and temperature fields were obtained. This convergence was monitored in two ways: by visual inspection of selected time-traces, and by checking the number of iterations needed by the BiCG solver, which drops to zero when the velocity and temperature field are the same in the new and old time step. By that time, the value of $Nu$ had also became time-invariant.

The progression in $Re$ was obtained by increasing the pressure drop in the source term of the momentum equation. Since the pressure drop is the independent variable, the calculated Reynolds number did not turn out to be an integer value. Other approaches could also be adopted, like to adjust the kinematic viscosity (Wang and Vanka, 1995), or to prescribe the Reynolds number first, and then adjust the pressure drop in order to obtain the desired mass flow and Reynolds number.

### *5.1.1. Sine-shaped channel*

For this geometry, the flow is first seen to separate at $Re = 24.9$. With further increase in $Re$ the recirculation bubble increases in size, and shifts downstream, with the last steady state observed at $Re = 175$. This result agrees with the numerical results of Wang and Vanka (1995), which predicted steady state at $Re = 167$, and unsteady periodic behavior at $Re = 200$, and the experimental observations of Nishimura et al. (1984, 1990), which qualitatively observed that the flow becomes unsteady when increasing $Re$ from 100 to 300.

For the heat transfer rate we observed that, in agreement with Wang and Vanka (1995), the Nusselt number does not increase significantly in the steady regime. In particular, $Nu = 7.8$ at $Re = 13.6$, and slightly increases with $Re$, reaching $Nu = 9.3$ at $Re = 175$. Therefore, at all $Re$ values investigated, the Nusselt number, for this geometrical configuration, is higher than the corresponding value, $Nu = 7.54$, for the parallel-plate channel. This means that, even for steady, low-$Re$ conditions, the sinusoidal channel provides a modest increase of heat transfer rate. However, as it will be summarized later, the pressure drop and consequently the friction factor, is consistently higher than that experienced in the parallel-plate channel.

Fig. 7 shows, for the sine-shaped channel, the calculated streamlines and temperature contours at a Reynolds number of 175.

### *5.1.2. Arc-shaped channel*

For this geometry, the flow already separates at $Re = 19.2$, where the recirculation zones are formed behind the sharp edges of the arc-shaped channel. By increasing the Reynolds number, the recirculation zones increase in size and shift downward, as it was also observed for the sine-shaped channel.

An unsteady regime was found, for the arc-shaped channel, at $Re = 84$, with the last steady state, obtained at $Re = 61$, illustrated in Fig. 8. Therefore, the transition to unsteady flow for the arc-shaped channel occurs at a lower Reynolds number than for the sinusoidal channel. This is the consequence of the fact that the edges of the arc-shaped channel are much sharper than the edges of the sine-shaped channel, and thus contribute to the formation, at lower $Re$ values, of an unstable jet-pattern, which easily becomes unsteady.

Notwithstanding three-dimensional effects, which could not be detected with our two-dimensional calculations, these findings qualitatively agree with the experimental visualizations of Nishimura et al. (1990), which observed that, for the arc-shaped passage, the flow becomes unsteady at $Re$ above 100, and that the onset of unsteadiness occurs at lower $Re$ values than in the case of sinusoidal walls.

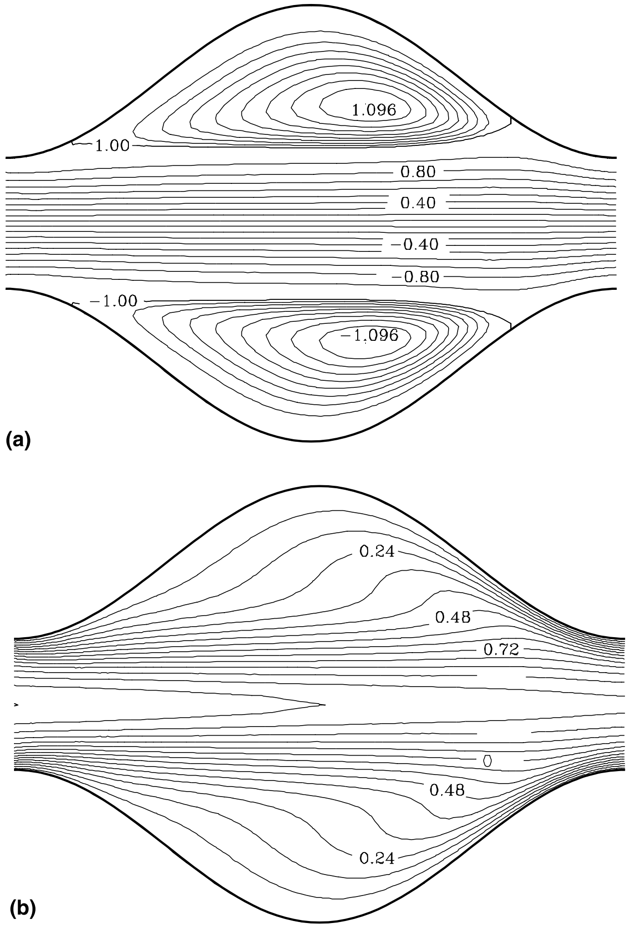

Fig. 7. Streamlines (a) and temperature contours (b) for the sinusoidal channel at $Re = 175$.

At $Re = 19.2$ the Nusselt number is equal to $Nu = 7.1$, than with the increase of $Re$ it decreases slightly, and reaches the minimum value of $Nu = 7.0$ at $Re = 32$. With further increase in $Re$, $Nu$ increases and reaches the value of $Nu = 7.3$ at $Re = 61$. For this configuration, at all Reynolds numbers the value of $Nu$ is consistently lower than the values obtained for the sinusoidal channel. It is also lower than the value of $Nu$ for the fully developed flow in a parallel-plate channel. This means that the arc-shaped channel does not provide any increase in heat transfer when operating in the steady flow regime, and yet there is the penalty of an increase in pressure drop.

The low heat transfer performances of the arc-shaped channel at steady, low $Re$ values, are, at least qualitatively, corroborated by the observations reported in Nishimura et al. (1990), where, by considering the analogy between heat and mass transfer, they found that the arc-shaped channel, up to $Re$ less than 55, is characterised by a lower mass transfer rate than sinusoidal walls.

### *5.2. Unsteady regime*

In the unsteady regime, once the flow and temperature fields reached statistical steady-state conditions, the calculations were continued for a sufficiently long time, until invariant values of time-averaged $Nu$ and $f$ were obtained.

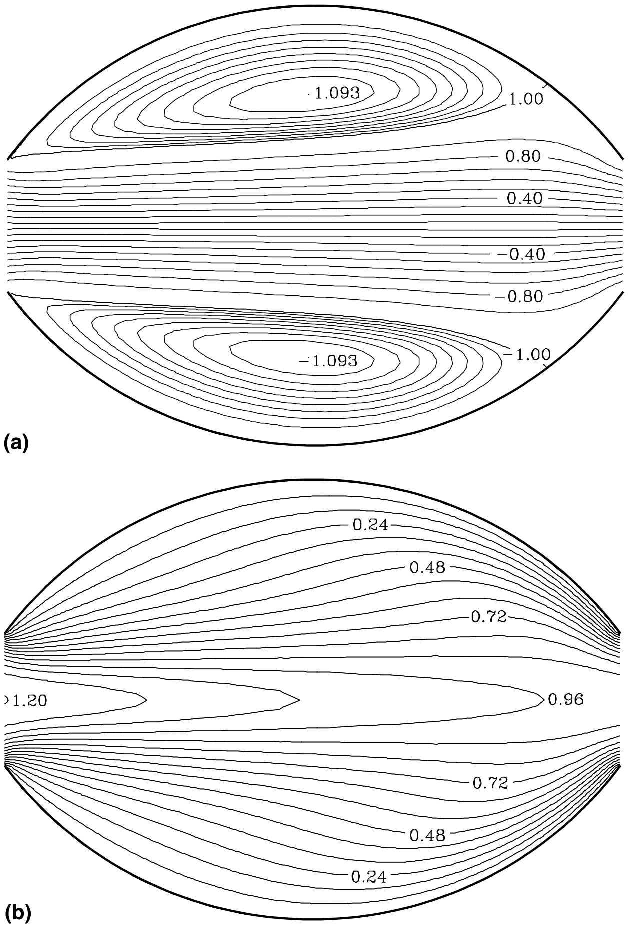

Fig. 8. Streamlines (a) and temperature contours (b) for the arc-shaped channel at $Re = 61$.

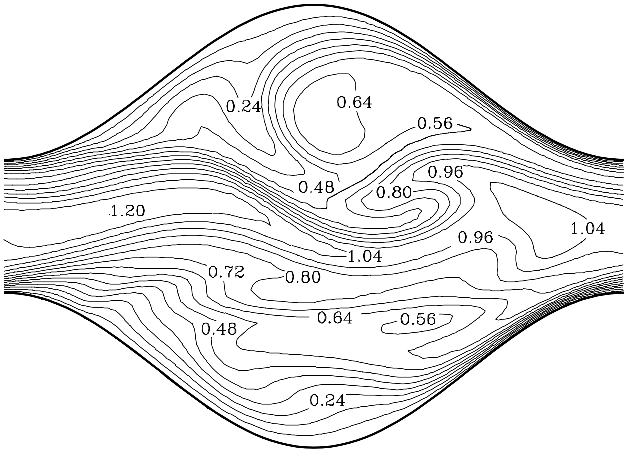

Fig. 9. Instantaneous temperature field for the sinusoidal channel in the unsteady regime at $Re = 412$.

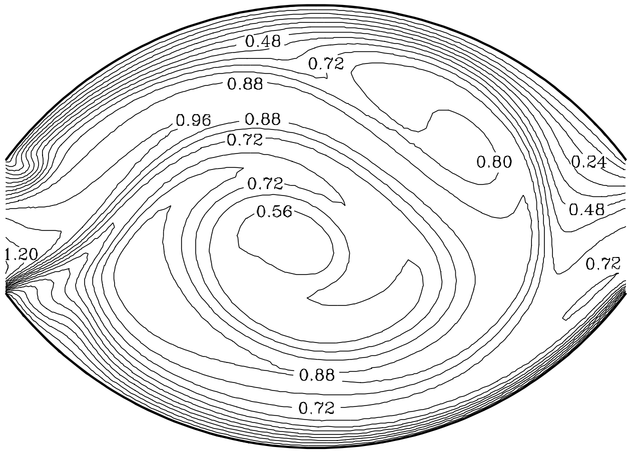

Fig. 10. Instantaneous temperature field for the arc-shaped channel in the unsteady regime at $Re = 226$.

### 5.2.1. *Sine-shaped channel*

As already stated, we have found that the bifurcation to an unsteady regime occurs at $Re > 175$. At $Re = 203$ the flow exhibits a periodic character. The time history of the velocity at one point in the domain, not reported here, approaches a limit cycle. As the Reynolds number is increased, a new characteristic frequency occurs, and the flow exhibits a quasi-periodic behavior. Further increase of $Re$ leads to a chaotic behavior. A snapshot of the temperature field in the unsteady flow regime is shown, for illustrative purposes, in Fig. 9 for $Re = 412$. It is clearly visible from the figure that several vortices coexist, which mix the cold fluid near the boundaries with the hot fluid from the core. This, in turn, increases the temperature gradients near the walls, producing, as a net effect, an increase in the heat transfer rate.

At $Re = 412$, which is the highest Reynolds number that we have calculated, the Nusselt number is $Nu = 20.2$, which is more than twice the maximum value of $Nu$ under steady conditions.

### 5.2.2. *Arc-shaped channel*

As already observed, the unsteady regime for the arc-shaped channel is reached at significantly lower Reynolds number than for the sinusoidal channel.

For this geometry of the flow passage, in the unsteady regime, the increase of the Nusselt number is somehow higher than that observed for the sinusoidal channel. For example, for the arc-shaped channel at $Re = 103$, the Nusselt number is $Nu = 13.6$, a value obtained, for the sine-shaped channel, at a higher Reynolds number, approximately $Re = 263$. It means that the arc-shaped channel provides higher increase of the heat transfer rate in the unsteady flow regime than the sinusoidal channel, though with the penalty of higher friction factors.

The instantaneous pattern of the temperature field is illustrated, for $Re = 226$, in Fig. 10, where the oscillating vortices are clearly recognizable, together with the higher temperature gradients at the walls.

### 5.3. *Summary of performance data*

The results obtained for both geometries are summarized in Fig. 11, which encompasses both steady and unsteady regimes, where the Nusselt number $Nu$ and the friction factor $f$, are given as a function of the Reynolds number. For comparison purposes, also the $Nu$ values obtained numerically by Wang and Vanka (1995) are plotted in Fig. 11(a), and they agree well with our results.

From the figure it is evident that, in comparison with the straight channel, the heat transfer increase, at low-$Re$ steady conditions, is very low for the sinusoidal channel, and is even slightly negative for the arc-shaped channel. The increase in

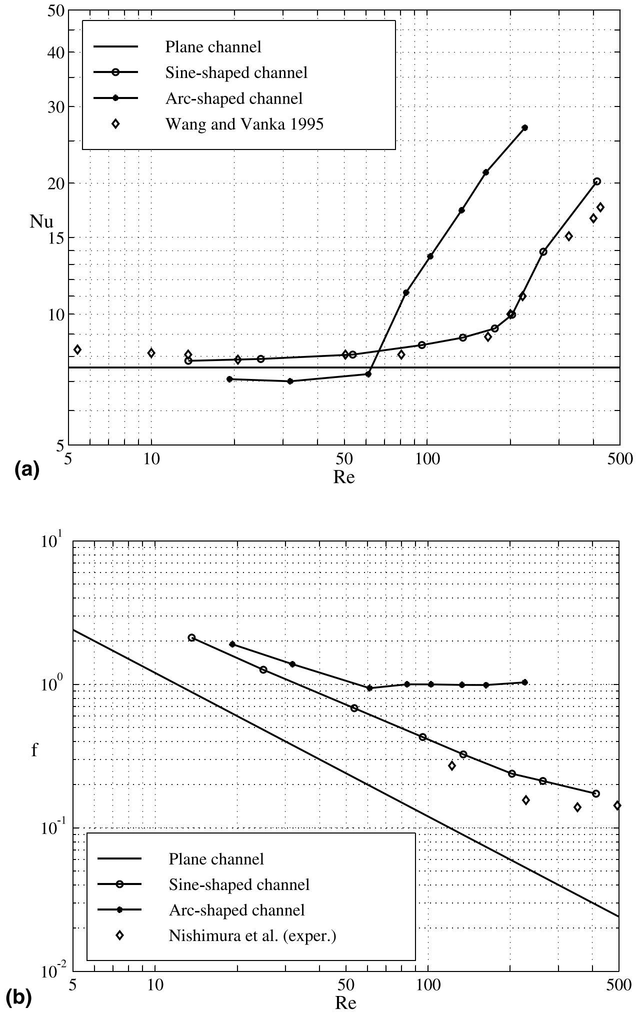

Fig. 11. Performance characteristics of the sinusoidal channel and arc-shaped channel as a function of the Reynolds number: (a) Nusselt number; (b) friction factor.

*Nu*, higher for the arc-shaped channel, becomes evident only in the unsteady regime.

The friction factor, for both geometries, is always higher, more than two times, than that of the parallel-plate channel in the steady, laminar regime. A significant increase of the friction factor, beyond the transition point, is visible in the curve where a rapid increase is observed. Some experimental data for the sine-shaped channel, taken from Nishimura et al. (1984), are also plotted in Fig. 11(b), and the trend, i.e., the change in slope, is correctly reproduced by our calculations, though the values of the friction factor are somehow overestimated. The friction factor of the arc-shaped channel is greater than that of the sinusoidal channel, also in the steady regime, whereas a reverse trend in *Nu* was predicted.

## 6. Conclusions

Fluid flow and heat transfer in periodic, corrugated channels, have been numerically investigated through a time-accurate, unstructured covolume method, for a fluid with $Pr = 0.7$, representative of air.

The geometrical configurations considered are a sinusoidal channel, which has been studied experimentally by Nishimura et al. (1984, 1990) and numerically by Wang and Vanka (1995), and an arc-shaped channel, also experimentally tested by Nishimura et al. (1990).

The results indicate that in the low Reynolds, steady regime, both geometries are ineffective, since they give heat transfer rates that are either slightly higher, for the sine channel, or even lower, for the arc-shaped channel, than that provided by the parallel-plate channel. However, beyond the critical value of the Reynolds number at which transition to an unsteady regime is observed, the heat transfer rate increases significantly, as a result of self-sustained oscillations.

The values of the friction factor, for both channels, are consistently higher than that of the parallel-plate channel, thus further indicating that corrugated channels are effective in enhancing the heat transfer rate only in unsteady regimes.

## Acknowledgements

Financial support for this research was provided by the Ministero dell' Università e della Ricerca Scientifica e Tecnologica – Progetto Nazionale 1997: *Termofluidodinamica Mono e Bifase* – and is gratefully acknowledged. A fellowship from the *Consortium for International Development of the University of Trieste* supported one of the authors (B. Ničeno) while on leave at University of Trieste, Italy, from the University of Rijeka, Croatia.

## References

Amon, C.H., Mikic, B.B., 1990. Prediction of convective heat transfer in self-sustained oscillatory flows. J. Thermophys. 4, 239–246.

Botta, N., Hempel, D., 1996. A finite volume projection method for the numerical solution of the incompressible Navier–Stokes equations on triangular grids. In: Benkhaldoun, F., Vilsmeier, R. (Eds.), Proceedings of the First International Symposium on Finite Volumes for Complex Applications – Problems and Perspectives. Rouen, France, pp. 467–476.

Cavendish, J.C., Hall, C.A., Porsching, T.A., 1992. Solution of incompressible Navier–Stokes equations on unstructured grids using dual tessellations. Int. J. Numer. Meth. Heat Fluid Flow 2, 483–502.

Cavendish, J.C., Hall, C.A., Porsching, T.A., 1994. A complementary volume approach for modeling three-dimensional Navier–Stokes equations using dual Delaunay/Voronoi tessellations. Int. J. Numer. Meth. Heat Fluid Flow 4, 329–345.

Despotis, G.K., Tsangaris, S., 1996. Fractional step method for solution of incompressible Navier–Stokes equations on unstructured triangular grids. Int. J. Numer. Meth. Fluids 20, 1273–1288.

Gresho, P.M., 1990. On the theory of semi-implicit projection method for viscous incompressible flow and its implementation via a finite element method that also introduces a nearly consistent mass matrix. Part 1: Theory. Int. J. Numer. Meth. Fluids 11, 587–620.

Hall, C.A., Cavendish, J.C., Frey, W.H., 1991. The dual variable method for solving fluid flow difference equations on Delaunay triangulations. Comput. Fluids 2, 145–164.

Hall, C.A., Porsching, T.A., 1996. A characteristic-like method for thermally expandable flow on unstructured triangular grids. Int. J. Numer. Meth. Fluids 22, 731–754.

Huser, A., Biringen, S., 1992. Calculation of two-dimensional shear-driven cavity flows at high Reynolds numbers. Int. J. Numer. Meth. Fluids 14, 1087–1109.

Hwang, Y.H., 1995a. Calculations of incompressible flow on a staggered triangular grid. Part I: Mathematical formulation. Numer. Heat Transfer, Part B 27, 323–336.

Hwang, Y.H., 1995b. Calculations of incompressible flow on a staggered triangular grid. Part II: Applications. Numer. Heat Transfer, Part B 27, 337–353.

Kakaç, S., Shah, R.K., Aung, W. (Eds.), 1980. Handbook of Single Phase Convective Heat Transfer. Wiley, New York, pp. 17.1–17.62.

Kobayashi, M.H., Pereira, J.M.C., Pereira, J.C.F., 1999. A conservative finite-volume second-order accurate projection method on hybrid unstructured grids. J. Comp. Phys. 150, 40–75.

Manson, J.R., Pender, G., Wallis, S.G., 1996. Limitations of traditional finite volume discretizations for unsteady computational fluid dynamics. AIAA J 34 (5), 1074–1076.

Murthy, J.Y., Mathur, S., 1997. Periodic flow and heat transfer using unstructured grids. Int. J. Numer. Meth. Fluids 25, 659–677.

Ničeno, B., 1997. EasyMesh v. 1.4 – Internet homepage: http://www-dinma.univ.trieste.it/nirftc/research/easymesh/.

Nicolaides, R.A., 1989. Flow discretization by complementary volume techniques. AIAA paper 89-1978, In: Proceedings of the Ninth AIAA CFD Meeting. Buffalo, New York.

Nicolaides, R.A., 1992. Direct discretization of planar Div–Curl problems. SIAM J. Numer. Anal. 29, 32–56.

Nishimura, T., Ohori, Y., Kawamura, Y., 1984. Flow characteristics in a channel with symmetric wavy-wall for steady flow. J. Chem. Eng. Jpn. 17, 466–471.

Nishimura, T., Murakami, S., Arakawa, S., Kawamura, Y., 1990. Flow observations and mass transfer characteristics in symmetrical wavy-walled channels at moderate Reynolds numbers for steady flow. Int. J. Heat Mass Transfer 33, 835–845.

Patankar, S.V., 1977. Fully developed flow and heat transfer in ducts having streamwise-periodic variations of cross-sectional area. ASME J. Heat Transfer 99, 180–186.

Perot, B., 2000. Conservation properties of unstructured staggered mesh schemes. J. Comp. Phys. 159, 58–89.

Rida, S., McKenty, F., Meng, F.L., Reggio, M., 1997. A staggered control volume scheme for unstructured triangular grids. Int. J. Numer. Meth. Fluids 25, 697–717.

Shah, R.K., London, A.L., 1978. Laminar Forced Convection in Ducts. Academic Press, New York.

Thomadakis, M., Leschziner, M., 1996. A pressure correction method for the solution of incompressible viscous flows on unstructured grids. Int. J. Numer. Meth. Fluids 22, 581–601.

Wang, G., Stone, K., Vanka, S.P., 1996. Unsteady heat transfer in baffled channels. ASME J Heat Transfer 118, 585–591.

Wang, G., Vanka, S.P., 1995. Convective heat transfer in wavy passages. Int. J. Heat Mass Transfer 38, 3219–3230.